
Explicitly Modeling Subcortical Vision with a Neuro-Inspired Front-End Improves CNN Robustness

Lucas Piper¹, Arlindo L. Oliveira^{1,2}, Tiago Marques³

¹INESC-ID Lisboa, Portugal

²IST Técnico Lisboa, Universidade de Lisboa, Portugal

³Breast Unit, Champalimaud Clinical Center, Champalimaud Foundation, Lisboa, Portugal
lucaspiper99[at]tecnico[dot]ulisboa[dot]pt

Abstract

Convolutional neural networks (CNNs) trained on object recognition achieve high task performance but continue to exhibit vulnerability under a range of visual perturbations and out-of-domain images, when compared with biological vision. Prior work has demonstrated that coupling a standard CNN with a front-end block (VOneBlock) that mimics the primate primary visual cortex (V1) can improve overall model robustness. Expanding on this, we introduce Early Vision Networks (EVNets), a new class of hybrid CNNs that combine the VOneBlock with a novel SubcorticalBlock, whose architecture draws from computational models in neuroscience and is parameterized to maximize alignment with subcortical responses reported across multiple experimental studies. Without being optimized to do so, the assembly of the SubcorticalBlock with the VOneBlock improved V1 alignment across most standard V1 benchmarks, and better modeled extra-classical receptive field phenomena. In addition, EVNets exhibit stronger emergent shape bias and overperform the base CNN architecture by 8.5% on an aggregate benchmark of robustness evaluations, including adversarial perturbations, common corruptions, and domain shifts. Finally, we show that EVNets can be further improved when paired with a state-of-the-art data augmentation technique, surpassing the performance of the isolated data augmentation approach by 7.3% on our robustness benchmark. This result reveals complementary benefits between changes in architecture to better mimic biology and training-based machine learning approaches.

1 Introduction

Convolutional neural networks (CNNs) have achieved remarkable performance across a range of object recognition benchmarks [NIPS2012_c399862d, simonyan2015deep, szegedy2014going, he2015deep, tan2020efficientnet], yet they remain vulnerable when faced with common corruptions [hendrycks2019benchmarking], domain shifts [geirhos2021partial, geirhos2022imagenettrained, geirhos2020accuracy], and adversarial perturbations [madry2019deep, goodfellow2015explaining]. These vulnerabilities not only limit deployment in real-world settings but also underscore fundamental disparities between computer vision models and primate vision [geirhos2022imagenettrained, geirhos2021partial]. In response, recent work has introduced biologically inspired models that integrate neuroscientific computations into CNN pipelines [Dapello2020.06.16.154542, cirincione2022implementing, pushpull2024, EVANS202296, 10.1007/978-3-031-44204-9_33]. A prominent example is the VOneNet family [Dapello2020.06.16.154542], which improves adversarial and corruption robustness by combining a biologically constrained front-end — the VOneBlock — to conventional CNN architectures. This block simulates processing in primate primary visual cortex (V1) via a

fixed-weight, empirically constrained Gabor filter bank (GFB), nonlinearities reflecting responses of V1 simple and complex cells, and a neural noise generator. While VOneNets represent a key step towards neurally-aligned vision models, they abstract away the hierarchical processing in the early visual system, notably omitting subcortical circuits such as the retina and lateral geniculate nucleus (LGN). This raises the question of whether incorporating more complete models of V1, solely by refining upstream processing to include explicit subcortical processing, yields further gains in robustness and alignment with biological vision.

To address this question, we present the following key contributions:

- We introduce a novel fixed-weight CNN front-end called the SubcorticalBlock designed to capture key computations in the retina and the LGN. This module is instantiated from neuroscientific models and is explicitly parameterized to produce responses aligned with a broad set of experimentally observed subcortical response properties.
- We introduce Early Vision Networks (EVNets), a new class of hybrid CNNs that combines two biologically-grounded modules — the VOneBlock and our new SubcorticalBlock — as a multi-stage front-end for a standard CNN architecture.
- We show that without any explicit optimization for V1 predictivity, EVNets improve neural and behavioral alignment with primate vision, outperforming both standard CNNs and VOneNets across multiple benchmarks. In particular, EVNets capture extra-classical RF phenomena more accurately, increase V1 predictivity and tuning property alignment, and better mimic human inductive biases through a stronger emergence of shape bias.
- We demonstrate that EVNets deliver enhanced robustness across a diverse battery of evaluations, including adversarial attacks, common image corruptions, and domain shifts, while maintaining similar accuracy on clean images.
- We show that EVNets trained with a state-of-the-art (SOTA) data augmentation technique yield additive improvements in robustness, highlighting the complementary effects of architectural priors and training-based strategies.

1.1 Related Work

Modeling subcortical vision. The Difference-of-Gaussian (DoG) model emerged as the foundational linear framework for characterizing spatial summation over the receptive field (RF) of subcortical cells [kuffler1953, Rodieck1965-yv]. Subsequent extensions modeled extra-classical RF properties, including contrast gain control and surround suppression [Shapley1978-dx, Solomon2006-zt]. Building on this, divisive normalization [Carandini2011-xb, Bonin2005-cu] and cascading linear-nonlinear (LN) models [MANTE2008625] improved subcortical predictivity by incorporating the interaction between different visual processing stages. More recently, CNNs outperformed prior models in predicting subcortical responses to visual stimuli [McIntosh2016].

Improving perturbation robustness. CNN robustness improvements have largely been driven by data augmentation techniques [hendrycks2020augmix, hendrycks2021faces, 10.1007/978-3-031-19806-9_36]. To this end, standard benchmarks evaluate models under image corruptions [hendrycks2019benchmarking] and alternative renditions [hendrycks2021faces, salvador2022imagenetcartoon, wang2019learning, geirhos2021partial, geirhos2022imagenettrained]. Recent work highlights that composing augmentations [hendrycks2020augmix, hendrycks2021faces, 10.1007/978-3-030-58580-8_4], especially when integrated with architectural changes [pushpull2024], forwards the SOTA under this regime. Notably, PRIME augmentation [10.1007/978-3-031-19806-9_36] samples semantically-aligned transformations from maximum entropy distributions. In parallel, the vulnerability of CNNs to white-box adversarial perturbations has catalyzed extensive research [madry2019deep, obfuscated-gradients, carlini2019evaluating] with adversarial training emerging as the dominant paradigm for improving robustness [madry2019deep].

Measuring alignment with primate vision. A growing suite of metrics has emerged to quantify the alignment between models and the primate vision [Marques2021.03.01.433495, Freeman2013, SchrimpfKubilius2018BrainScore, Schrimpf2020integrative]. Metrics such as shape bias [geirhos2022imagenettrained] have been instrumental in measuring model-human behavioral alignment, while a parallel line of research emphasizes representational alignment through the

comparison of model tuning properties to those observed in neural data [Marques2021.03.01.433495, Freeman2013, olaiya2022measuring]. Complementing these efforts, the BrainScore platform [SchrimpfKubilius2018BrainScore, Schrimpf2020integrative] provides a unified benchmark that integrates neural recordings and behavioral data across multiple visual cortical areas, including V1, V2, V4, and IT, alongside behavioral and task-driven metrics.

Building neuro-inspired models. Introducing biological computations into CNNs has consistently enhanced their robustness to input perturbations [EVANS202296, 10.1007/978-3-031-44204-9_33, pushpull2024, 10.1007/s00521-020-04751-8, Dapello2020.06.16.154542]. Gains have been observed with convolutional layers aligned to early visual RFs [EVANS202296, 10.1007/978-3-031-44204-9_33], push-pull inhibition motifs inspired by V1 [pushpull2024, 10.1007/s00521-020-04751-8], and by introducing the VOneBlock [Dapello2020.06.16.154542, cirincione2022implementing]. Besides improving adversarial and corruption robustness, VOneNets achieved improved accuracy in V1 predictivity, and, when combined with V1 divisive normalization, further sharpened alignment with V1 response properties and corruption robustness [cirincione2022implementing, olaiya2022measuring]. Finally, the systematic composition of hallmark V1 computations into CNNs recently achieved SOTA performance on explaining V1 predictivity and tuning properties [pogoncheff2023explaining].

2 Methods

Inspired by the hierarchical organization of early visual processing culminating in V1, we introduce EVNets, a new family of neuro-inspired CNNs that build upon the VOneNet framework. EVNets incorporate modular fixed-weight front-ends that reflects the functional stages of the early primate visual pathway (Fig. 1). This architecture comprises three key components: the SubcorticalBlock, modeling response characteristics of foveal neurons in the retina and the LGN; a variant of the VOneBlock, which models classical RF properties of V1 neurons; and a standard CNN back-end architecture. Together, the front-end blocks instantiate a composite cascading LN model of early cortical vision. EVNets adopt a spike-count formulation, abstracting over temporal dynamics, focusing solely on spatial encoding. The EVNet operates over a 7deg field-of-view (FoV), reduced from the 8deg used in the original VOneBlock [Dapello2020.06.16.154542]. We also extend the GFB to higher spatial frequencies (SFs), improving alignment with the SF tuning properties of primate V1 [DEVALOIS1982545] (cf. Supplementary Material A for an overview of VOneNets and our modifications). We trained three random seeds for both the VOneNet and the EVNet model families using a ResNet50 [he2015deep] back-end architecture (cf. Supplementary Material D.2 for a study on back-end generalization). All models were trained on the ImageNet-1k dataset [NIPS2012_c399862d], with clean accuracy evaluated on the standard validation split.

2.1 Architecture

The SubcorticalBlock simulates spatial summation over the RF of parvocellular (P) and magnocellular (M) cells, processing them as separate parallel pathways. To account for both classical and extra-classical properties, each pathway comprises a light adaptation stage, a DoG convolutional layer, a contrast normalization stage, and a noise generator that simulates subcortical noise statistics.

DoG convolution. Spatial summation over the RF and center-surround antagonism is modeled by incorporating a set of DoG filters described by

$$w_{\text{DoG}}(x, y) = \exp\left(-\frac{x^2 + y^2}{r_c^2}\right) - (k_s/k_c) \exp\left(-\frac{x^2 + y^2}{r_s^2}\right), \quad (1)$$

where r_c and r_s are the center and surround radii, and k_s/k_c is the peak contrast sensitivity ratio. We simulate biological color-opponent pathways characteristic of the different types of cells, with the P-cell stream incorporating red-green, green-red, and blue-yellow opponency, whereas M cells reflect achromaticity by incorporating a DoG filter with no color tuning [10.3389/fneur.2021.661938, Wiesel1966-zq].

Light adaptation. To mimic the subcortical mechanism of light adaptation [Carandini2011-xb, MANTE2008625, berardino2018eigendistortions], we introduce a biologically inspired module that performs global luminance normalization through a parameterized variant of the classical Naka-Rushton function [Naka1966-uo]. This transformation modulates the input \mathbf{x} as

$$\mathbf{x}_{\text{LA}} = \frac{\mathbf{x}^\gamma}{\mathbf{x}^\gamma + \bar{\mathbf{x}}^\gamma} - b_{\text{LA}}, \quad (2)$$

where x_{LA} is the light-adapted input, $\bar{\mathbf{x}}$ denotes the spatial average of the input, γ controls the nonlinearity of the response, and $b_{\text{LA}} = 1/2$ is a centering bias that ensures a null output for inputs matching the global mean.

Contrast normalization. To model the adaptive gain control mechanisms characteristic of early visual processing [Carandini2011-xb, Bonin2005-cu, MANTE2008625, RaghavanENEURO.0515-22.2023, Mante2005-kc], we introduce a contrast normalization stage that normalizes activations by a local estimate of stimulus contrast. Formally, the normalized response is computed by

$$\mathbf{x}_{\text{CN}} = \frac{\mathbf{x}_{\text{DoG}}}{(c_{50} + \sqrt{\mathbf{x}_{\text{DoG}}^2 * \mathbf{w}_{\text{CN}}})^n}, \quad (3)$$

where \mathbf{x}_{DoG} denotes the pre-normalized activation, \mathbf{w}_{CN} is a Gaussian kernel defining the contrast integration pooling window, c_{50} is a semi-saturation constant controlling sensitivity, and n governs the strength of the nonlinearity.

Push-pull pattern. The canonical push-pull pattern, emerging from the antagonistic interaction between ON- and OFF-center cells in early visual circuits, can be functionally approximated by subtracting rectified responses of opposite polarity pathways [doi:10.1126/science.8191289, Hirsch1998-lq]. Assuming ON and OFF cells of the same type share identical spatial profiles and gain, their RFs differ only in polarity. Under this assumption, since Equation 3 is antisymmetric with respect to \mathbf{x}_{DoG} , the contrast-normalized responses of the ON and OFF pathways, $\mathbf{x}_{\text{CN}}^\pm$, would satisfy $\mathbf{x}_{\text{CN}}^+ = -\mathbf{x}_{\text{CN}}^-$. Thus, applying rectification to both signals and computing their differences gives

$$\max(\mathbf{x}_{\text{CN}}^+, 0) - \max(-\mathbf{x}_{\text{CN}}^+, 0) = \mathbf{x}_{\text{CN}}^+. \quad (4)$$

Accordingly, our implementation bypasses explicit rectification and subtraction steps, instead operating directly on the signed contrast-normalized signal to improve computational efficiency without sacrificing functional fidelity.

Noise Generator. Neuronal responses in the primate visual system exhibit trial-to-trial variability with distinct stochastic signatures across processing stages. In V1, spike count variability closely follows a Poisson distribution, where the variance is equal to the mean [Softky1993-te]. In this case, the Fano factor, defined as the ratio between the variance and the mean is equal to one. Conversely, subcortical neurons exhibit sub-Poisson variability, characterized by a spike count variance that grows slower than the mean [doi:10.1152/jn.00058.2022, doi:10.1152/jn.01171.2003]. To faithfully capture this hierarchical structure of neural noise, we implement a dual-source noise injection mechanism in which we add independent Gaussian noise to each units of both front-end blocks. This noise is calibrated to maintain an overall variability with a unit Fano factor, while trial-to-trial activations at the VOneBlock output exhibit heteroskedasticity consistent with V1 measurements [Softky1993-te]. Prior to noise injection, unit activations are linearly rescaled such that their mean response to a stimulus aligns with the empirically observed spike count of the corresponding primate neuronal population over a 50-ms integration window [doi:10.1152/jn.00058.2022, Dapello2020.06.16.154542].

2.2 Subcortical-Aligning Parameterization

Despite the wealth of empirical data on primate LGN and the existence of various fitted models [Carandini2011-xb, Bonin2005-cu, MANTE2008625, RaghavanENEURO.0515-22.2023,

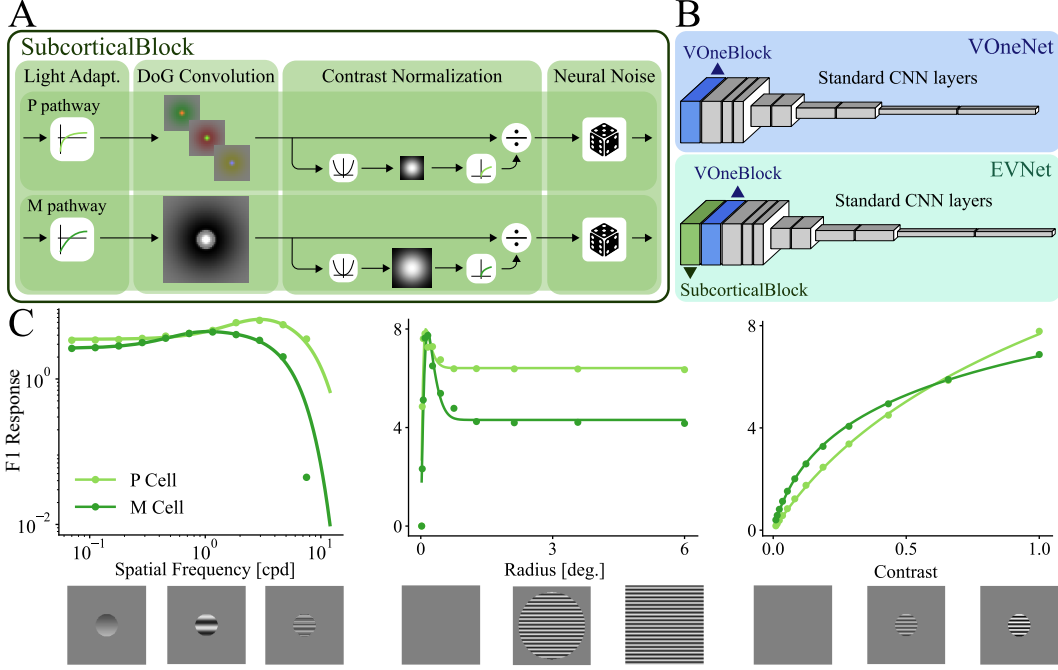


Figure 1: **Simulating primate early visual processing as CNN front-end blocks.** **A** The SubcorticalBlock integrates two parallel processing pathways for P and M cells with a light-adaptation layer, a DoG convolutional layer, a contrast-normalization layer and a neural noise generator. **B** Both VOneNets and EVNets comprise an initial block designed to simulate the visual system, followed by a standard CNN architecture. VOneNets include a VOneBlock and EVNets include both a SubcorticalBlock and a VOneBlock. **C** SF, size, and contrast tuning curves (left to right) for two example subcortical neurons with example frames from the drifting gratings stimulus set shown below. Markers indicate the F1 component of the cell response and the solid line depicts the fitted response functions used for parameterizing response properties (cf. Supplementary Material E.2). Notably, the SubcorticalBlock exhibits hallmark LGN phenomena, including contrast saturation and surround suppression, with stronger modulation observed in M cells.

Mante2005-kc], the heterogeneity of modeling approaches across studies limits the direct reuse of parameters in the SubcorticalBlock, while complicating synthesis from the broader literature. To address this, we introduce a novel neurophysiologically-constrained hyperparameter tuning strategy designed to produce responses that best match the mean neuronal response properties of an LGN neuronal population taken from prior studies and modeling strategies. Specifically, we selected a total of $N = 6$ different response property distributions measured at foveal LGN to ensure alignment in SF tuning, size tuning, and contrast sensitivity. The individual properties are: center, surround, excitation and inhibition radii [Solomon338, Rodieck1965-yv, Sceniak1999], suppression index [Solomon338] and saturation index [RaghavanENEURO.0515-22.2023].

We conducted a series of *in silico* experiments, presenting each cell with drifting gratings, quantifying each response property through the first harmonic (F1) of the cell’s response. We then performed hyperparameter search via Bayesian optimization [10.1007/3-540-07165-2_55], minimizing the loss

$$\mathcal{L} = \sum_{i=1}^N \left[\log_2 \left(\frac{R_i(\mathbf{f}_{1,i})}{\bar{r}_i} \right) \right]^2. \quad (5)$$

For each response property i , \bar{r}_i is the mean of the empirical response property distribution, $\mathbf{f}_{1,i}$ is a vector of F1 responses produced by the SubcorticalBlock cell when subjected to the experiment-specific stimulus set, and R_i maps the F1 responses to the response property. This mapping often involved an intermediate model-fitting step, with the response property computed from the fitted parameters. Figure 1C shows the F1 responses of both P and M cells, example frames of the stimulus

set used for each experiment and response model curves obtained at convergence (cf. Supplementary Material E.2 for in-depth description of experiment methodology).

2.3 Model Evaluation

Alignment with primate vision. The emergence of shape bias was measured using a cue-conflict dataset [geirhos2022imagenettrained] that combines the shapes and textures of ImageNet samples using style transfer [7780634]. To quantify the correspondence between model internal representations and biological V1 responses, we assessed the activations from the first computational block of each model using two complementary BrainScore [SchrumpfKubilius2018BrainScore, Schrumpf2020integrative] benchmarks: V1 neural predictivity [Freeman2013] and V1 response property [Marques2021.03.01.433495]. V1 neural predictivity evaluates the degree to which model-derived features can account for the variance in primate V1 neuronal responses via partial least squares (PLS) regression. In contrast, V1 response property quantifies RF tuning similarity by comparing the distributions of 22 neural response properties — extracted from the same first-block activations — to empirical V1 distributions. These properties span 7 functional categories: orientation tuning, SF tuning, response selectivity, RF size, surround modulation, texture modulation, and response magnitude.

Robustness evaluation. To quantify robustness, we report a mean Robustness Score, defined as the mean top-1 accuracy across a diverse set of common corruptions, adversarial attacks, and domain shifts. To assess whether EVNets offer complementary gains to SOTA robustness training methods, we trained both a standard ResNet50 and our EVNet model using PRIME [10.1007/978-3-031-19806-9_36]. As an additional baseline, we included adversarial training with an L_∞ constraint of $\|\delta\|_\infty = 4/255$ [robustness] (AT_{L_∞}). Additional training and evaluation details are provided in Supplementary Material E.

Image corruptions. We evaluated model corruption robustness by measuring top-1 accuracy on the ImageNet-C dataset [hendrycks2019benchmarking], which comprises 75 distinct corrupted variants of the ImageNet validation set. These corruptions are organized into 15 types applied at five severity levels, reflecting a specific real-world image degradation. The corruption types are further grouped into four broad categories: noise, blur, weather, and digital perturbations.

Domain shifts. To assess each model’s generalization under domain shifts, we averaged top-1 accuracies across five ImageNet-derived datasets that focus on renditions partially addressable by early visual processing mechanisms. Specifically, we used ImageNet-R [hendrycks2021faces], ImageNet-Cartoon [salvador2022imagenetcartoon], ImageNet-Drawing [salvador2022imagenetcartoon], ImageNet-Sketch [wang2019learning], and the 16-class Stylized-ImageNet [geirhos2021partial, geirhos2022imagenettrained] (Stylized₁₆-ImageNet). Each dataset introduces representational changes such as abstraction, stylization, or domain-specific distortions while preserving the underlying semantic structure.

Adversarial attacks. Following the protocol in Dapello et al. [Dapello2020.06.16.154542], we evaluated robustness to white-box adversarial attacks by applying untargeted Projected Gradient Descent (PGD) [madry2019deep] on the same 5000 images of the ImageNet validation set. Attacks were carried out under L_∞ , L_2 and L_1 norm constraints and the perturbation budgets used were $\|\delta\|_\infty \in [1/1020, 1/255, 4/255, 16/255]$, $\|\delta\|_2 \in [0.15, 0.6, 1.2, 2.4]$ and $\|\delta\|_1 \in [40, 160, 640, 2560]$. We used 16 PGD iterations with step size of $\|\delta\|_p/8$. Given the stochastic nature of our models, we employed the reparameterization trick [Kingma2014] during sampling to enable stable gradient-based learning. To account for the dual noise injection, we also performed Monte Carlo sampling to accurately estimate gradients under noise [obfuscated-gradients], averaging 32 samples per PGD iteration. Due to computational constraints, adversarial evaluations were conducted using two random seeds. Additional control experiments are provided in Supplementary Material C.1.

Ablation studies. We performed a set of model ablations to assess the contribution of specific components to robustness. Details about these experiments are presented in Supplementary Material D.

3 Results

3.1 EVNets Improve Neuronal and Behavioral Alignment with Primate Vision

We evaluated whether coupling the SubcorticalBlock with the VOneBlock improved alignment with primate V1. As illustrated in Figure 2, the inclusion of the SubcorticalBlock upstream of the VOneBlock introduces hallmark extra-classical RF response properties absent from the VOneBlock alone. In particular, we observe an increased surround suppression in the size tuning curve and clear contrast saturation in the contrast-sensitivity curve.

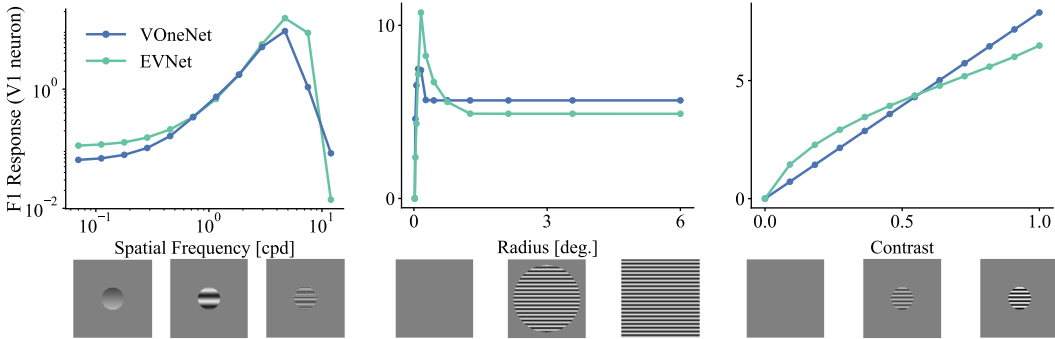


Figure 2: **Subcortical preprocessing improves explainability of extra-classical RF properties in V1.** SF, size, and contrast tuning curves (left to right) for an example neuron in the VOneBlock with and without subcortical preprocessing (M cell). Example frames from the drifting gratings stimulus set are shown below. V1 cells in isolation exhibit predominantly classical response properties but when coupled with subcortical processing exhibit emergent behaviors consistent with those empirically observed, such as enhanced surround modulation and contrast saturation[doi:10.1152/jn.00692.2001, SCLAR19901].

Motivated by these observations, we used the BrainScore platform [SchrimpfKubilius2018BrainScore, Schrimpf2020integrative] to quantitatively evaluate V1 alignment. As shown in Table 1, EVResNet50 achieves higher scores on nearly all response properties, besides improving both the mean response property score and V1 neural predictivity scores. Notably, the highest gains are observed for the surround modulation and RF size tuning — both associated with the increased surround suppression. A tradeoff in SF tuning and texture modulation is observed, which can be attributed to the fact that no changes were done to the GFB to account for the upstream processing.

Table 1: **EVResNet50 overperforms baselines on V1 neural predictivity, V1 response property alignment, and shape bias.** BrainScore [SchrimpfKubilius2018BrainScore, Schrimpf2020integrative] V1 alignment scores and shape bias [geirhos2022imagenettrained] for ResNet50, VOneResNet50, and EVResNet50. Values indicate mean \pm SD ($n = 3$ seeds).

Model	V1 Predict.	V1 Resp. Prop.	V1 Response Properties							
			Orient. Tuning	SF Tuning	RF Size	Surround Mod.	Texture Mod.	Resp. Select.	Resp. Magn.	Shape Bias [%]
ResNet50 [he2015deep]	.271 \pm .002	.637 \pm .008	.822 \pm .027	.754 \pm .026	.214 \pm .002	.389 \pm .023	.792 \pm .028	.621 \pm .010	.865 \pm .012	18.8 \pm 1.2
VOneResNet50	.375 \pm .002	.754 \pm .006	.859 \pm .005	.969 \pm .001	.482 \pm .041	.373 \pm .003	.919 \pm .004	.792 \pm .003	.884 \pm .002	31.6 \pm 1.2
EVResNet50	.379 \pm .002	.808 \pm .001	.881 \pm .002	.913 \pm .004	.719 \pm .005	.635 \pm .007	.736 \pm .009	.839 \pm .003	.933 \pm .012	46.3 \pm 1.2

Among the suite of metrics used to assess alignment between models and primate visual behavior, shape bias has emerged as a particularly informative proxy of human-aligned inductive biases and out-of-domain (OOD) generalization [geirhos2022imagenettrained, geirhos2021partial]. Motivated by the hypothesis that shape bias may originate as early as early visual computations, we evaluated shape bias in EVNets (Tab. 1) and observed a substantial increase of 27.5% relative to the standard

ResNet50 and of 14.7% relative to the VOneNet model, suggesting that EVNets may confer not only improved neuronal alignment but also behavioral traits more consistent with primate perception.

3.2 EVNets Improve Robustness Across an Aggregate Benchmark

When tested on clean images (Tab. 2), our VOneNets variant achieves a 1.2% improvement over the original VOneNet [Dapello2020.06.16.154542], while EVNets maintain the same reported accuracy. We further examined whether the increased alignment of EVNets with primate vision, also leads to improved robustness.

Image corruptions. Across most corruption categories and in terms of mean corruption accuracy, EVNets consistently outperformed both VOneNets and the base ResNet50, which only retained an advantage in weather corruptions. Notably, the most pronounced gains were observed on noise corruptions, where EVNets overperformed VOneNets by 2.5% while effectively preserving the same cumulative Fano factor as VOneNets.

Table 2: **EVResNet50 overperforms baselines on most image corruption types and on mean corruption accuracy.** Clean and corrupted top-1 accuracies averaged across severities and corruptions for ResNet50, VOneResNet50 and EVResNet50. Values indicate mean \pm SD ($n = 3$ seeds).

Model	Corruption Types					
	Mean [%]	Noise [%]	Blur [%]	Weather [%]	Digital [%]	Clean [%]
ResNet50 [he2015deep]	38.8 \pm 0.5	29.2 \pm 0.6	34.6 \pm 0.4	36.1\pm0.5	49.5 \pm 0.6	75.4\pm0.1
VOneResNet50	40.4 \pm 0.1	35.9 \pm 0.5	34.8 \pm 0.1	32.6 \pm 0.1	52.2 \pm 0.1	72.9 \pm 0.1
EVResNet50	41.5\pm0.1	38.4\pm0.7	37.0\pm0.2	31.9 \pm 0.1	52.7\pm0.1	71.7 \pm 0.1

Domain shifts. Table 3 summarizes our OOD generalization results. EVNets consistently outperforms both the baseline ResNet50 and VOneNets across the majority of benchmarks, also surpassing these baselines on the mean domain shift accuracy. The sole exception is ImageNet-Sketch, where the base ResNet50 exhibits a marginal advantage.

Table 3: **EVResNet50 overperforms baselines on most domain shift datasets and on overall mean domain shift accuracy.** Top-1 accuracies on ImageNet-{Cartoon, Drawing, R, Sketch, Stylized₁₆} for ResNet50, VOneResNet50 and EVResNet50. Values indicate mean \pm SD ($n = 3$ seeds).

Model	Mean [%]	Cartoon [%]	Drawing [%]	R [%]	Sketch [%]	Stylized ₁₆ [%]
ResNet50 [he2015deep]	33.4 \pm 0.2	51.2 \pm 0.7	20.9 \pm 0.6	35.4 \pm 0.1	23.3\pm0.1	36.3 \pm 1.2
VOneResNet50	37.1 \pm 0.4	55.5 \pm 0.2	30.5 \pm 0.4	37.5 \pm 0.1	23.1 \pm 0.3	38.8 \pm 1.1
EVResNet50	38.7\pm0.1	57.8\pm0.3	33.5\pm0.3	38.1\pm0.3	23.0 \pm 0.3	41.0\pm0.3

Adversarial attacks. Given the lower clean accuracy of EVNets and prior findings that downstream stochasticity is the main contributor to VOneNet’s adversarial robustness [Dapello2020.06.16.154542], we anticipated a modest reduction in robustness relative to VOneNets. Interestingly, while VOneNets maintained the highest mean accuracy across all perturbation norms and attack strengths (Tab. 4), EVNets exhibited a smaller gap between clean and adversarial accuracy. Moreover, EVNets provided the greatest gains under stronger attacks, particularly within the L_2 and L_1 norm constraints, suggesting a potential link between training under inherited noise and robustness under larger perturbations.

Table 5 summarizes these results and presents the Robustness Score for the evaluated models.

3.3 Combining EVNets with Data Augmentation Provides Cumulative Gains

In our evaluation of the Robustness Score for the EVResNet50 with PRIME data augmentation (Tab. 5), we observe the same performance gain as when PRIME is added to the standard ResNet50,

Table 4: **EVResNet50 overperforms base ResNet50 model under a range of adversarial perturbations and increases robustness to higher L_1 and L_2 norm constraints, when compared to VOneNets.** Top-1 accuracies for the ResNet50, VOneResNet50 and EVResNet50 models. Values indicate mean \pm SD ($n = 2$ seeds).

Model	Mean [%]	$\ \delta\ _\infty$				$\ \delta\ _2$				$\ \delta\ _1$			
		$\frac{1}{1020}$ [%]	$\frac{1}{255}$ [%]	$\frac{4}{255}$ [%]	$\frac{16}{255}$ [%]	0.15 [%]	0.6 [%]	1.2 [%]	2.4 [%]	40 [%]	160 [%]	640 [%]	2560 [%]
ResNet50 [he2015deep]	8.5 \pm 0.3	24.1 \pm 0.7	0.6 \pm 0.0	0.2 \pm 0.0	0.2 \pm 0.0	37.6 \pm 1.0	2.1 \pm 0.3	0.2 \pm 0.0	0.2 \pm 0.0	34.2 \pm 0.7	1.9 \pm 0.2	0.2 \pm 0.0	0.2 \pm 0.1
VOneResNet50	26.6 \pm 0.1	62.0 \pm 0.1	29.5 \pm 0.1	1.1 \pm 0.1	0.0 \pm 0.0	66.7 \pm 0.3	45.0 \pm 0.8	4.6 \pm 0.1	0.0 \pm 0.0	65.8 \pm 0.5	39.8 \pm 0.4	4.2 \pm 0.1	0.0 \pm 0.0
EVResNet50	25.9 \pm 0.0	60.4 \pm 0.3	29.2 \pm 0.0	0.9 \pm 0.1	0.0 \pm 0.0	63.2 \pm 0.3	40.6 \pm 0.4	8.7 \pm 0.2	3.9 \pm 0.1	60.0 \pm 0.1	33.7 \pm 0.4	6.6 \pm 0.3	3.8 \pm 0.1

exhibiting near-linear cumulative improvements. Furthermore, when comparing these results with those obtained by augmenting a ResNet50 with adversarial training, no configuration surpasses the additive gains achieved by the EVResNet50 trained with PRIME.

Table 5: **EVResNet50 achieves a higher Robust Score than ResNet50 and VOneResNet50 and, when coupled with PRIME, surpasses SOTA data augmentation approaches.** Clean and perturbed top-1 accuracies for the ResNet50, VOneResNet50 and EVResNet50 models; for ResNet50 with two data augmentation approaches: AT_{L_∞} and PRIME; and EVResNet50 with PRIME. Values indicate mean \pm SD ($n = 2$ seeds).

Model	Robust. Score [%]	Perturbations			Clean [%]
		Adversarial [%]	Corrupt. [%]	Domain Shift [%]	
ResNet50 [he2015deep]	27.0 \pm 0.1	8.6 \pm 0.3	39.1 \pm 0.3	33.3 \pm 0.1	75.4 \pm 0.1
VOneResNet	34.6 \pm 0.1	26.6 \pm 0.1	40.4 \pm 0.2	36.9 \pm 0.1	72.9 \pm 0.1
EVResNet	35.4 \pm 0.0	25.9 \pm 0.0	41.5 \pm 0.1	38.7 \pm 0.1	71.7 \pm 0.1
ResNet50 + AT_{L_∞} [robustness]	34.5	31.5	32.5	39.5	62.4
ResNet50 + PRIME [10.1007/978-3-031-19806-9_36]	34.2	14.8	52.6	42.6	76.0
EVResNet50 + PRIME	41.5 \pm 0.2	27.4 \pm 0.2	52.6 \pm 0.0	44.7 \pm 0.3	73.0 \pm 0.1

3.4 Not All Components of the SubcorticalBlock Contribute to Improving Robustness

Though ablating components of the SubcorticalBlock in most cases reduced model robustness (cf. Supplementary Material D.1), removing the M cell pathway had minimal effect.

4 Discussion

A central challenge in computer vision lies in designing models that are robust to diverse image perturbations. This is not only an essential property for real-world deployment but also for approximating biological vision. In this work, we present a new family of neuro-inspired CNNs that not only display enhanced robustness across a broad spectrum of perturbations but also achieve stronger alignment with primate vision. In contrast to our approach, the current literature has relied on combining CNN architecture with isolated components of early visual processing, such as RF filters [10.1007/978-3-031-44204-9_33, EVANS202296] and normalization schemes [NIPS2012_c399862d, 5459469]. Our SubcorticalBlock, however, draws directly from computational neuroscience, with parameters constrained by decades of empirical findings. The EVNet architecture introduces a modular, cascading model of V1 that incorporates stage-specific architectural priors, offering a compelling alternative to V1-inspired CNN paradigms. While EVNets do not entirely solve the longstanding problem of robust generalization, our results underscore the critical importance of subcortical processing in shaping early visual representations. Notably, we

demonstrate that meaningful improvements to V1 modeling can be achieved by exclusively refining upstream stages. The cumulative gain shown by combining the SubcorticalBlock with the VOneBlock reveal a biologically-plausible potential for compositionality in inductive biases, where each module targets distinct axes of visual invariance, together producing synergistic improvements in OOD generalization. Specifically, while the SubcorticalBlock primarily encodes invariance to luminance and contrast, the VOneBlock focuses more on spatial and polarity invariance. Finally, we show that integrating biologically-inspired architectures with standard data augmentation techniques leads to synergistic improvements in robustness. This suggests that neuroscience-driven inductive biases and machine learning heuristics are not mutually exclusive, but can in fact be complementary.

While the observed robustness gains are compelling, there are also some trade-offs. Specifically, our model abstracts subcortical processing by instantiating only four channels that reflect the average spatial response profiles observed in the LGN, rather than attempting to capture the full heterogeneity of subcortical cells. A related limitation of our approach is that M-cell pathway contributes only marginally to downstream performance (cf. Supplementary Material D.1), which, while being in line with the classical view of M cells contribution to the ventral stream, also presents inconsistencies with current literature [CANARIO2016110]. Additionally, enhancements in perturbation robustness are consistently accompanied by modest reductions in clean image accuracy — a common tension in robustness research [pushpull2024, Dapello2020.06.16.154542]. Moreover, the slight decrease in adversarial robustness may point to a deeper dissociation between inherited and V1-intrinsic noise in the VOneBlock architecture, opening a promising avenue for future investigation. It is important to mention that the noise injected at the SubcorticalBlock has considerably lower dimensionality than that in V1 (4 channels vs. 512 channels, across the spatial map). Beyond these considerations, subsequent work could examine the generalization of these robustness benefits across diverse training distributions. In terms of V1 alignment, it is important to note that no changes were made in the VOneBlock to accommodate upstream processing. We opted for this approach to facilitate model comparison and because there were no drastic changes to VOneBlock responses other than the improvement of extra-classical RF phenomena. However, alignment to V1 decreased in a couple of benchmarks which is likely due to the interaction of the two modules. Future work, could explore how the GFB in the VOneBlock should change to reflect subcortical preprocessing. Finally, as EVNets modulate only subcortical extra-classical phenomena, it remains an open question whether incorporating V1-inspired normalization mechanisms could further enhance V1 alignment.

Broader impact. This work advances computer vision by providing a biologically-plausible alternative to the increasingly popular, but non-biologically-based, transformer architectures [NIPS2017_3f5ee243, dosovitskiy2021an]. By simulating early visual processes, we narrow the gap between human and machine vision, fostering greater robustness while enhancing transparency and interpretability, besides a potential to reduce bias and enhance accessibility in underrepresented settings. Nevertheless, fully replicating human vision remains a challenge, requiring further research and more elaborate modeling. It is important to acknowledge that some of the foundational studies informing our study involved animal research. While these studies have contributed vastly to our understanding of the visual system, they also highlight the ethical considerations. In line with contemporary ethical standards, we recognize and underscore the importance of minimizing harm and using alternative methods whenever possible. This work illustrates how leveraging existing biological data can inform model development, potentially reducing reliance on new animal experiments.

Acknowledgments

This work was supported by the project Center for Responsible AI reference no. C628696807-00454142, financed by the Recovery and Resilience Facility, by project PRELUNA, grant PIDC/CCIINF/4703/2021, and by Fundação para a Ciência e Tecnologia (FCT), under grant UIDB/50021/2020.

Supplementary Material

A VOneNets

VOneNets [Dapello2020.06.16.154542] are convolutional neural networks (CNNs) augmented with a biologically-inspired, fixed-weight front-end simulating primary visual cortex (V1), termed the VOneBlock. This front-end is structured as a linear–nonlinear–Poisson (LNP) cascade [RUST2005945], incorporating a Gabor filter bank (GFB) [Jones1987-dy], nonlinearities for both simple and complex cells [Adelson:85], and a stochastic spiking mechanism modeling neuronal variability [Softky1993-te] (cf. Fig. A1). The GFB parameters are sampled from empirical distributions of orientation preference, spatial frequency (SF) tuning, and receptive field (RF) size [DEVALOIS1982545, DEVALOIS1982531, ringach2002spatial_dstructure]. The channels are split evenly between simple and complex cells, and a Poisson-like noise generator is applied to emulate spiking variability. The full implementation is available at <https://github.com/dicarlo1ab/vonetnet> under a GNU General Public License v3.0.

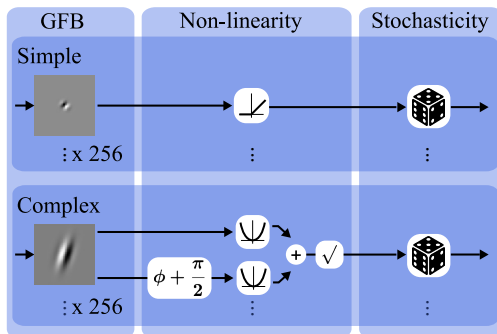


Figure A1: **VOneNets simulate V1 processing upstream of standard CNNs.** Each VOneNet incorporates a biologically-constrained front-end, the VOneBlock, preceding a conventional CNN. The VOneBlock consists of a fixed-weight Gabor filter bank (GFB) parameterized by empirical distributions, nonlinearities emulating simple and complex cell responses, and a stochastic component that injects Poisson-like noise to mimic V1 neuronal variability. Adapted from Baidya et al. [baidya2021combining].

To construct the VOneNet variants, we replaced the initial block of each base architecture with the VOneBlock, along with a channel-matching bottleneck layer to maintain architectural compatibility between the front-end and the downstream convolutional stack. Consistent with the original VOneResNet50 model [Dapello2020.06.16.154542], we replaced a single convolutional layer, batch normalization, nonlinearity, and a max-pooling operation. When using an EfficientNet-B0, we substituted the initial convolution, batch normalization, and activation with the VOneBlock. For VOneResNet50, we preserved the original configuration of 512 channels within the VOneBlock, allocating 256 channels to each cell type (simple and complex). However, given the reduced channel dimensionality in the EfficientNet-B0 where the second stage expects only 32 channels, in contrast to 64 in ResNet50 we downscaled the VOneBlock accordingly, employing 128 channels per cell type.

We modified the VOneBlock by adjusting the field of view (FoV) to 7deg (down from the original 8deg) and increased the spatial frequency range of the GFB to 0.5 – 8.0 cpd (from 0.5 – 5.6cpd). Additionally, to maintain consistency with upstream processing, we configured the GFB to uniformly sample a single channel from the input, regardless of any preceding subcortical transformations. Finally, to ensure methodological consistency in the spike-based activation regime across both the SubcorticalBlock (cf. Section E.2) and the VOneBlock, we imposed a unified temporal integration window of 50ms. In alignment with Table C2 of Dapello et al. [Dapello2020.06.16.154542], we applied a linear scaling factor to the VOneBlock outputs such that the mean evoked response to a batch of natural images from ImageNet matched the target stimulus response of 0.655 spikes. This variant of the VOneBlock was used on the both the VOneNet and the EVnet models described in this study.

B Primate Vision Alignment

Shape-bias. In contrast to humans, who predominantly rely on shape cues for object recognition, ImageNet-trained CNNs have been shown to exhibit a strong bias toward texture-based representations [geirhos2022imagenettrained]. Measuring shape bias thus serves as a proxy for alignment with human inductive biases. We evaluate this using the cue conflict dataset from Geirhos et

al. [geirhos2022imagenettrained], where images contain conflicting shape and texture cues (e.g., a cat-shaped image with elephant texture). While humans tend to classify by shape, ImageNet-trained CNNs often prefer texture. A model’s shape bias is computed as the proportion of shape-consistent predictions out of all shape- or texture-consistent responses.

BrainScore. The BrainScore platform [SchrimpfKubilius2018BrainScore, Schrimpf2020integrative] is a standardized benchmarking suite for evaluating how brain-like artificial neural networks (ANNs) are. In the context of object recognition, BrainScore compares model activations against neural recordings from primate visual areas and human behavioral data. For early visual processing, V1 predictivity is quantified via the FreemanZiemba2013 [Freeman2013] neural benchmark, while response properties in V1 are assessed using the Marques2020 [Marques2021.03.01.433495] benchmark. BrainScore aggregates multiple such benchmarks into a composite score that reflects a model’s alignment with neural and behavioral patterns observed in biological systems. Researchers can submit their models for evaluation at <https://www.brain-score.org/>.

V1 Predictivity. To predict model’s ability to predict single-neuron responses in V1, we employed a dataset [Freeman2013] comprising responses from 102 V1 neurons to 450 unique 4deg image patches, spanning both naturalistic textures and noise stimuli. Predictivity was measured as the explained variance using partial least squares (PLS) regression under a 10-fold cross-validation scheme

V1 Response Properties. Marques et al. [Marques2021.03.01.433495] introduced a novel model-to-brain comparison framework that bypasses conventional fitting procedures, instead relying on *in silico* neurophysiology to establish direct, one-to-one correspondences between artificial and V1 neurons. By probing models with canonical stimulus sets such as drifting gratings and texture pattern, the method quantifies alignment through a normalized similarity metric grounded in the Kolmogorov-Smirnov distance, capturing the distributional match of neural response properties. Critically, this framework enables rigorous benchmarking against prior neurophysiological studies without requiring raw recordings, effectively transforming existing literature into executable V1-aligning tests. In total, this method focuses on 22 distinct response characteristics, organized into seven functional domains: orientation tuning, spatial frequency tuning, receptive field size, surround modulation, texture modulation, response selectivity, and response magnitude. Table B1 presents all individual response properties along with the scores obtained for the ResNet50, the VOneResNet50 and EVResNet50 models.

C Image Perturbations

C.1 Adversarial Attacks

To evaluate white-box robustness, we employed Projected Gradient Descent (PGD) [madry2019deep] on top of a subset of 5000 images from the ImageNet validation split. PGD is a widely adopted first-order attack that has proven effective against biologically inspired models such as VOneNets [Dapello2020.06.16.154542]. We selected this attack due to its scalability to large datasets (e.g., 5k ImageNet samples), and its compatibility with deterministic inference pipelines, which avoids the pitfalls of stochastic defenses that may artificially degrade attack success rates [Dapello2020.06.16.154542]. We run PGD for 16 iterations, where each step follows the update rule:

$$\mathbf{x}^{t+1} = \mathcal{P}_{\mathbf{x}+\mathcal{S}} \left(\mathbf{x}^t + \alpha \operatorname{sgn} \left(\nabla_{\mathbf{x}^t} \mathcal{L}(\theta, \mathbf{x}^t, \mathbf{y}) \right) \right),$$

where \mathbf{x}^t denotes the adversarial input at iteration t , \mathcal{L} is the cross-entropy loss function, and $\mathcal{P}_{\mathbf{x}+\mathcal{S}}$ projects back onto the perturbation set \mathcal{S} centered at the clean input \mathbf{x} . Under an L_∞ threat model, \mathcal{S} corresponds to a box constraint, while for L_1 or L_2 norms with a perturbation budget ϵ , the gradient direction is rescaled at each iteration to have the respective norm α , and the projection ensures the final adversarial input \mathbf{x}_{adv} satisfies $\|\mathbf{x}_{\text{adv}} - \mathbf{x}\|_p \leq \epsilon$. We used a step size of $\alpha = \|\mathbf{x}_{\text{adv}} - \mathbf{x}\|_p / 8$ and performed a total of 12 attacks carried out under L_∞ , L_2 and L_1 norm constraints at four perturbation budgets each: $\|\delta\|_\infty \in [1/1020, 1/255, 4/255, 16/255]$, $\|\delta\|_2 \in [0.15, 0.6, 1.2, 2.4]$

Table B1: **EVResNet50 overperforms baselines on V1 response property alignment.** Brain-Score [SchrimpfKubilius2018BrainScore, Schrimpf2020integrative] V1 alignment scores for ResNet50, VOneResNet50, and EVResNet50. Values indicate mean \pm SD ($n = 3$ seeds).

Category	Resp. Property	Models		
		ResNet50 [he2015deep]	VOneResNet50	EVResNet50
Orientation	Orientation Selective	0.975 \pm 0.024	0.999\pm0.001	0.994 \pm 0.003
	Circ. Variance (CV)	0.818\pm0.011	0.742 \pm 0.013	0.807 \pm 0.009
	Orth./Pref. Ratio	0.855\pm0.023	0.717 \pm 0.014	0.755 \pm 0.008
	CV Bandwidth Ratio	0.740 \pm 0.024	0.763 \pm 0.005	0.813\pm0.007
	Pref. Orientation	0.943 \pm 0.046	0.985\pm0.004	0.976 \pm 0.015
	Orth./Pref.-CV Diff.	0.766 \pm 0.016	0.885\pm0.004	0.857 \pm 0.008
	Or. Bandwidth	0.659 \pm 0.086	0.922 \pm 0.010	0.964\pm0.006
Spatial Frequency	Peak SF	0.551 \pm 0.047	0.961\pm0.002	0.957 \pm 0.005
	SF Bandwidth	0.826 \pm 0.019	0.962\pm0.006	0.899 \pm 0.007
	SF Selective	0.886 \pm 0.053	0.983\pm0.005	0.881 \pm 0.007
Response Selectivity	Texture Selective	0.678 \pm 0.008	0.800 \pm 0.004	0.821\pm0.006
	Modulation Ratio	0.349 \pm 0.009	0.737 \pm 0.002	0.875\pm0.005
	Texture Var. Ratio	0.794\pm0.014	0.703 \pm 0.011	0.720 \pm 0.006
	Texture Sparseness	0.663 \pm 0.032	0.927 \pm 0.002	0.939\pm0.003
RF Size	Grating Sum. Field	0.272 \pm 0.005	0.547 \pm 0.016	0.705\pm0.009
	Surround Diameter	0.156 \pm 0.000	0.361 \pm 0.015	0.733\pm0.003
Surround Mod.	Surround Sup. Index	0.389 \pm 0.023	0.373 \pm 0.003	0.635\pm0.007
Texture Modulation	Abs. Texture Mod. Idx.	0.978\pm0.019	0.942 \pm 0.004	0.845 \pm 0.009
	Texture Mod. Idx.	0.606 \pm 0.040	0.897\pm0.011	0.627 \pm 0.010
Response Magnitude	Max. Texture	0.939 \pm 0.002	0.906 \pm 0.010	0.948\pm0.005
	Max. DC	0.873\pm0.053	0.824 \pm 0.008	0.902 \pm 0.023
	Max. Noise	0.783 \pm 0.018	0.923 \pm 0.006	0.949\pm0.011

and $\|\delta\|_1 \in [40, 160, 640, 2560]$. We used the Adversarial Robustness ToolBox v1.17.1 [art2018] to conduct all the attacks.

Due to the inherent stochasticity in our models, special considerations were necessary to enable gradient-based adversarial optimization. We first applied the reparameterization trick [Kingma2014], which permits gradient flow through stochastic nodes by expressing random variables as deterministic functions of noise. To obtain reliable gradient estimates for PGD, we further adopted the approach of Athalye et al. [obfuscated-gradients], replacing ∇f with an average over multiple stochastic forward passes. Specifically, we estimate gradients as

$$\nabla f \approx \frac{1}{N} \sum_{i=1}^N \nabla_i f,$$

where each $\nabla_i f$ corresponds to a gradient computed using an independent Monte Carlo sample. We set $N = 32$, increasing the number of samples compared to prior work on VOneNets (which used $N = 10$) to compensate for the additional sources of noise introduced in our architecture.

To verify the reliability of our adversarial evaluation pipeline, we conducted a suite of sanity checks on a 500-image subset from the ImageNet validation set. In line with the recommendations of Athalye et al. [obfuscated-gradients] and Carlini et al. [carlini2019evaluating], we confirmed that top-1 accuracy decreases monotonically as a function of perturbation strength across all norm constraints (Tab. 4). Additionally, we also verified that increasing the number of gradient samples in the Monte Carlo approximation did not lead to a substantial increase in attack success (Fig. C1), further supporting the completeness of our threat model.

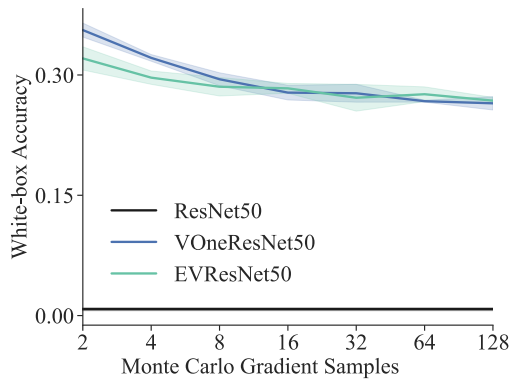


Figure C1: **Increasing the number of Monte Carlo gradient samples (k) has limited impact on white-box attack effectiveness.** White-box PGD accuracy ($\|\delta\|_\infty = 1/255$, 16 iterations) evaluated on 500 images. Increasing k from 32 to 128 leads to only marginal decreases in accuracy for both VOneResNet50 and EVResNet50, indicating that additional samples do not substantially strengthen the attack. Lines indicate the mean accuracy and shaded regions denote SD ($n = 3$ seeds).

C.2 Image Corruptions



Figure C2: **Examples of common image corruptions from the ImageNet-C dataset at intermediate severity (level 3)** The first row shows the original image and three noise corruptions; the second row displays blur corruptions; the third row presents weather-related corruptions; and the fourth row illustrates digital corruptions.

The ImageNet-C dataset [hendrycks2019benchmarking] consists of 15 different corruption types, each at 5 levels of severity for a total of 75 different perturbations applied to validation images of the ImageNet validation split. Accuracy improvement on these datasets should be indicative of model robustness gains, given that it comprises, in total, 75 diverse corruptions. The individual corruption types are Gaussian noise, shot noise, impulse noise, defocus blur, glass blur, motion blur, zoom blur, snow, frost, fog, brightness, contrast, elastic transform, pixelated, and JPEG compression.

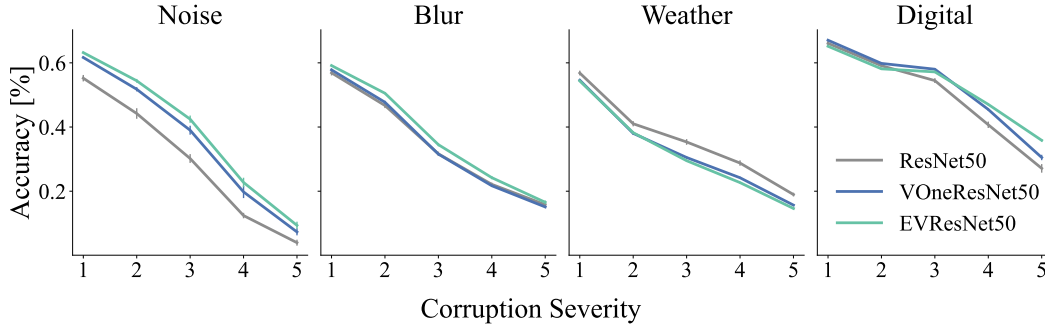


Figure C3: **EVResNet50 enhances robustness to noise, blur, and digital corruptions.** Top-1 accuracy across corruption severity levels for the four categories of common corruptions: noise, blur, weather, and digital. Solid lines indicate the mean performance; error bars denote SD ($n = 3$ seeds)

The individual corruption types are grouped into 4 categories: noise, blur, weather, and digital effects. Examples of image corruptions are presented in Figure C2. The ImageNet-C dataset is publicly available at <https://github.com/hendrycks/robustness> under Creative Commons Attribution 4.0 International.

C.3 Domain Shifts

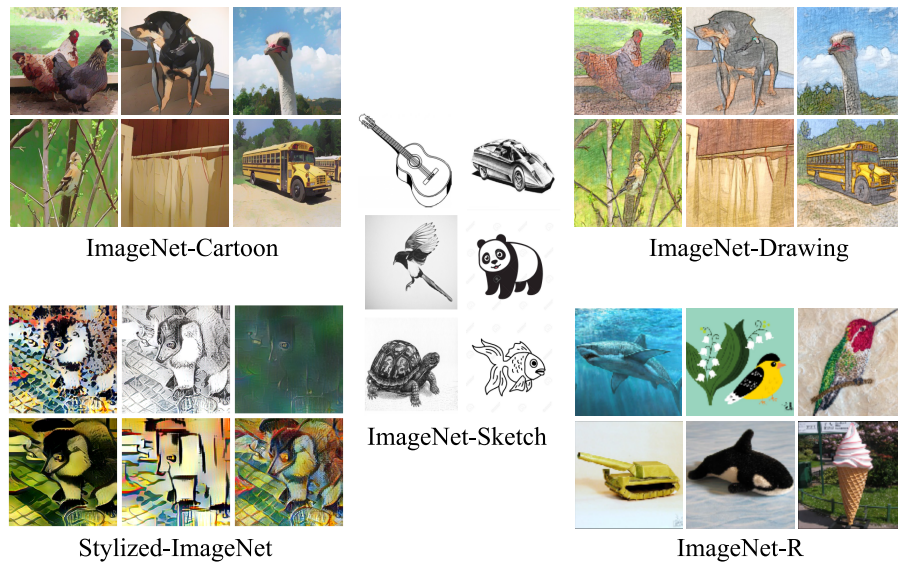


Figure C4: **Examples from domain shift benchmark datasets derived from ImageNet.** **ImageNet-Cartoon** (adopted from Salvador and Oberman [salvador2022imagenetcartoon]) features object representations in cartoon style. **ImageNet-Drawing** (adopted from Salvador and Oberman [salvador2022imagenetcartoon]) includes images rendered as colored pencil-like hand drawings. **ImageNet-Sketch** (adopted from Wang et al. [wang2019learning]) consists of black-and-white sketches emphasizing contours. **Stylized-ImageNet** (adopted from Geirhos et al. [geirhos2022imagenettrained]) applies replaces the original textures with those of random paintings. **ImageNet-R** (adopted from Hendrycks et al. [hendrycks2021faces]) contains various renditions of ImageNet classes, including painting, cartoon, origami, toy, embroidery, and sculpture styles.²

²This figure includes images adapted from multiple sources for academic illustration purposes under fair use. All images are property of their respective authors or datasets.

ImageNet-R The ImageNet-R dataset [hendrycks2021faces], consists of a curated set of 200 classes from the ImageNet validation set. This dataset includes 30,000 images featuring renditions in various artistic styles, such as paintings, sketches, and cartoons, designed to test a model’s ability to generalize beyond natural image statistics. ImageNet-R is publicly available at <https://github.com/hendrycks/imagenet-r>.

ImageNet-Cartoon & ImageNet-Drawing The ImageNet-Cartoon and ImageNet-Drawing datasets [salvador2022imagenetcartoon], are two domain shift benchmarks derived from the ImageNet validation set by applying label-preserving style transformations. ImageNet-Cartoon contains images transformed into cartoon-like renditions using a GAN-based framework [9157493], while ImageNet-Drawing comprises colored pencil sketch versions of the same images created via an image processing pipeline [10.5555/2330147.2330161]. These datasets challenge models to generalize beyond natural image statistics, revealing significant accuracy drops—on average 18 and 45 percentage points, respectively—when standard ImageNet-trained models are evaluated. Both datasets are publicly available at <https://zenodo.org/records/6801109> under Creative Commons Attribution 4.0 International.

ImageNet-Sketch. The ImageNet-Sketch dataset [wang2019learning] is a large-scale benchmark designed to evaluate OOD generalization in image classification. It contains 50,000 black-and-white sketch-style images, with 50 images for each of the 1,000 classes in the ImageNet validation set, collected independently using keyword queries like “sketch of [class name]”. Unlike perturbation-based datasets, ImageNet-Sketch represents a significant domain shift in both texture and color, challenging models trained on natural images to rely on global structure rather than local textural cues. The dataset is publicly available at <https://www.kaggle.com/datasets/wanghaohan/imagenetsketch>.

Stylized₁₆-ImageNet. Stylized-ImageNet [geirhos2022imagenettrained] is created by introducing different painting styles into ImageNet images through Adaptive Instance Normalization style transfer [huang2017arbitrary]. While texture cues are replaced by those in the paintings, overall shape is preserved. Since the original dataset was introduced primarily for training purposes and models exhibited extremely low performance, we instead used a subset of Stylized-ImageNet as used in Geirhos et al. [geirhos2021partial]. This subset focuses on 16 basic categories (e.g., airplane, dog) that are supersets of 227 ImageNet classes within the WordNet hierarchy [10.1145/219717.219748]. We followed the same approach as the original article, where the probability distribution over ImageNet classes is mapped to this 16-class distribution by averaging the probabilities of corresponding fine-grained classes. This 16-class Stylized ImageNet along with the code for probability aggregation is publicly available at <https://github.com/bethgelab/model-vs-human>.

D Additional Experiments

Given the robustness gains observed on domain shifts and image corruptions with our EVResNet50 model, we conducted a series of ablation tests to assess the contribution of individual components to this improved performance. These experiments allowed us to isolate and understand the roles of specific elements in enhancing robustness. Furthermore, to validate the adaptability of our front-end block, we integrated it into a different backbone architecture, EfficientNet-B0, and evaluated its performance across the same robustness benchmarks.

D.1 SubcorticalBlock Ablation Study

We removed four components from the EVResNet50 model to evaluate their individual contributions: the M cell pathway, the contrast normalization layer, the light adaptation layer, and the subcortical noise. When removing subcortical noise, we ensured that the cortical noise at the end of the VOneBlock remained Poisson-distributed, consistent with the original VOneNets implementation. Despite some tradeoffs within individual corruption categories, no EVNet variants with removed components exhibited an increase in mean corruption accuracy (Tab. D1). As seen in VOneNets [Dapello2020.06.16.154542], stochasticity was the primary factor driving the drop in clean accuracy. Both light adaptation and contrast normalization contributed to robustness, with contrast normalization providing a slightly greater benefit. Interestingly, despite our efforts in explicitly

Table D1: **EVResNet50 overperforms ablations on most image corruption types and on mean corruption accuracy.** Clean and corrupted top-1 accuracies averaged across severities and corruptions for EVResNet50 and four ablation tests. Values indicate mean \pm SD ($n = 2$ seeds).

Model	Mean [%]	Corruption Types					Clean [%]
		Noise [%]	Blur [%]	Weather [%]	Digital [%]		
EVResNet50	41.5\pm0.1	38.4 \pm 0.7	37.0 \pm 0.2	31.9 \pm 0.1	52.7 \pm 0.1	71.7 \pm 0.1	
– M Cells	41.4 \pm 0.2	38.6\pm0.1	36.7 \pm 0.2	32.2 \pm 0.1	52.3 \pm 0.2	71.7 \pm 0.0	
– Subcort. Noise	41.2 \pm 0.0	36.6 \pm 0.6	35.9 \pm 0.2	33.7\pm0.5	53.4\pm0.2	72.9\pm0.4	
– Light Adaptation	40.9 \pm 0.1	34.5 \pm 0.3	36.4 \pm 0.3	32.7 \pm 0.1	53.4\pm0.0	72.3 \pm 0.1	
– Contrast Norm.	40.6 \pm 0.3	38.1 \pm 1.0	37.4\pm0.1	29.3 \pm 0.0	51.5 \pm 0.1	70.4 \pm 0.2	

modeling the main foveal subcortical pathways, the M cell pathway did not impact mean corruption accuracy at all, though some minor tradeoffs were observed across different corruption types.

Across all domain shift datasets, no model outperformed the full EVResNet50 (Tab. D2), although the variant without the M cell pathway achieved the same mean robustness accuracies. As with the corruption robustness results, replacing our dual noise approach with a single cortical noise injection led to a slight decrease in performance. Both normalization mechanisms contributed to OOD generalization, with light adaptation playing a more prominent role in this setting, in contrast to the corruption robustness tests where contrast normalization had a marginally greater impact.

Table D2: **EVResNet50 overperforms ablations on most domain shift datasets and on overall mean domain shift accuracy.** Top-1 accuracies on ImageNet-{Cartoon, Drawing, R, Sketch, Stylized₁₆} for EVResNet50 and four ablations. Values indicate mean \pm SD ($n = 2$ seeds).

Model	Mean [%]	Cartoon [%]	Drawing [%]	R [%]	Sketch [%]	Stylized ₁₆ [%]
EVResNet50	38.7\pm0.1	57.8 \pm 0.3	33.5 \pm 0.3	38.1 \pm 0.3	23.0 \pm 0.3	41.0\pm0.3
– M Cells	38.7\pm0.4	58.4\pm0.1	34.1\pm0.1	38.1 \pm 0.2	23.4 \pm 0.3	39.5 \pm 1.6
– Subcort. Noise	38.2 \pm 0.3	58.0 \pm 0.2	32.2 \pm 0.4	38.1 \pm 0.0	23.9\pm0.4	38.8 \pm 0.6
– Light Adaptation	38.0 \pm 0.0	56.6 \pm 0.5	33.0 \pm 0.1	38.3\pm0.2	23.0 \pm 0.1	39.1 \pm 0.4
– Contrast Norm.	38.6 \pm 0.3	57.4 \pm 0.1	34.0 \pm 0.3	38.0 \pm 0.1	22.5 \pm 0.1	41.0\pm1.9

D.2 EVNet Backend Generalization

Similarly to the results obtained with EVResNet50, the EVEfficientNet-B0 model consistently outperforms the base EfficientNet-B0 across most corruption categories, as well as in mean corruption accuracy, as shown in Table D3. However, this improvement comes with a greater relative drop in clean image accuracy compared to the ResNet50-based models. This steeper drop likely reflects architectural differences in sensitivity to input statistics. EfficientNet-B0 employs compound scaling and aggressive architecture search to optimize performance specifically for standard ImageNet inputs [[tan2020efficientnet](#)], making it more susceptible to deviations introduced by our biologically inspired preprocessing. In contrast, ResNet50, with its more generic design appears to be more adaptable to altered input distribution.

When evaluated on out-of-distribution datasets, EVEfficientNet-B0 surpasses the base model on all benchmarks, as reported in Table D4, which contrasts with the ResNet50 results where the base model achieved better performance on ImageNet-Sketch.

E Implementation Details

E.1 Grating Experiments

When tuning the SubcorticalBlock and when measuring its response properties, we presented 12 frames of drifting sine-wave gratings with phase shifts of 30 degrees in the interval $[0, 360[$ degrees.

Table D3: **EVEfficientNet-B0 overperforms base EfficientNet-B0 on most image corruption types and on mean corruption accuracy.** Clean and corrupted top-1 accuracies averaged across severities and corruptions for EVEfficientNet-B0 and EfficientNet-B0. Values indicate mean \pm SD ($n = 2$ seeds).

Model	Mean [%]	Corruption Types				Clean [%]
		Noise [%]	Blur [%]	Weather [%]	Digital [%]	
EfficientNet-B0 [tan2020efficientnet]	30.2 \pm 0.4	18.7 \pm 0.2	26.6 \pm 0.0	29.1\pm0.3	40.8 \pm 1.2	68.1\pm0.1
EVEfficientNet-B0	34.3\pm0.0	31.2\pm0.0	30.2\pm0.3	26.2 \pm 0.4	44.4\pm0.1	62.7 \pm 0.0

Table D4: **EVEfficientNet-B0 overperforms EfficientNet-B0 on all domain shift datasets.** Top-1 accuracies on ImageNet-{Cartoon, Drawing, R, Sketch, Stylized₁₆} for EfficientNet-B0 and EVEfficientNet-B0. Values indicate mean \pm SD ($n = 2$ seeds).

Model	Mean [%]	Cartoon [%]	Drawing [%]	R [%]	Sketch [%]	Stylized ₁₆ [%]
EfficientNet-B0 [tan2020efficientnet]	28.9 \pm 0.2	40.2 \pm 0.4	17.1 \pm 0.5	29.9 \pm 0.2	17.3 \pm 0.5	40.0 \pm 0.7
EVEfficientNet-B0	34.2\pm0.1	51.1\pm0.3	27.8\pm0.1	31.8\pm0.0	17.5\pm0.0	43.3\pm0.1

Grating orientation was set to horizontal and the diameter, SF and contrast was chosen to most accurately replicate the response-property studies used for tuning (see Table B1 for the reference studies from which the stimulus set properties were taken). The background area not covered by the grating was set to 50% gray. To characterize the response properties of the VOneBlock, we adopted the same experimental paradigm as detailed above.

E.2 SubcorticalBlock Implementation

To parameterize the fixed weights of the SubcorticalBlock, we developed a novel tuning strategy that optimizes alignment with average neuronal response properties of SF tuning, size tuning, and contrast sensitivity, using Bayesian optimization. Table E5 shows the reference values and values obtained values for the six subcortical response properties. This procedure was applied independently to the P and M pathways within the SubcorticalBlock. While several hyperparameters were directly optimized, Gaussian kernel sizes were indirectly determined by computing the kernel size necessary to elicit 75% of the their total integrated response. Specifically, this formulation was used with the surround Gaussian in the DoG kernel and with the Gaussian kernel of Contrast Normalization layer.

Table E5: **Reference and tuned response property values for the SubcorticalBlock.** Response property values specific to P and M cells used to tune the SubcorticalBlock, shown alongside reference values from the original studies from which they were sourced. Six response properties were used for tuning: center, surround, excitation and inhibition radii; suppression index; and saturation index.

Resp. Property	Reference		SubcorticalBlock	
	P cells	M cells	P cells	M cells
Center Radius [deg] [Solomon338]	0.042	0.063	0.042	0.066
Surround Radius [deg] [Solomon338]	0.279	0.602	0.162	0.565
Excitation Radius [deg] [Solomon338]	0.236	0.289	0.070	0.116
Inhibition Radius [deg] [Solomon338]	0.564	0.869	0.312	0.411
Suppression Index [Solomon338]	0.808	0.719	0.813	0.539
Saturation Index [RaghavanENEURO.0515-22.2023]	0.095	0.365	0.200	0.470

Search space. When defining the search space for each variable in our Bayesian optimization framework, our primary objective was to minimize the introduction of inductive biases by employing search spaces as broad as feasible. In many cases, this was straightforward — for instance, we constrained parameters like the semisaturation constant, c_{50} to lie within physically meaningful

bounds. However, for parameters such as the center and surround radii of the DoG filters, the radius of the Gaussian used in the contrast normalization layer, and the ratio of peak contrast sensitivity, we adopted a more heuristic approach. Specifically, we drew on values reported in the neuroscience literature to inform the bounds of the search space. For the DoG center and surround radii, we defined symmetric search intervals of centered around values reported in the reference study to which we aimed to maximize alignment [Solomon338]. Similarly, the bounds for the normalization radius were guided by reported relationships between the suppressive field and the surround Gaussian [Bonin2005-cu]. The same principle was applied to the contrast sensitivity ratio [CRONER19957]. Table E6 provides a comprehensive overview of all parameters tuned, including the corresponding search bounds and the literature references used to guide their selection, where applicable.

Table E6: **Hyperparameter search space for the SubcorticalBlock.** Minimum and maximum bounds used in the Bayesian optimization for each hyperparameter of the SubcorticalBlock: center radius of the DoG (r_c); surround radius of the DoG (r_s); peak contrast sensitivity ratio (k_s/k_c); light adaptation nonlinearity constant (γ); contrast normalization pooling radius (r_{CN}); semisaturation constant (c_{50}); and contrast normalization exponent (n). For a subset of these hyperparameters, literature references were used to inform the choice of search bounds.

Layer	Hyperparam.	P cells		M cells		Reference
		Min.	Max.	Min.	Max.	
Light Adapt.	γ	0.01	2.0	0.01	2.0	—
DoG Conv.	r_c [deg]	0.034	0.050	0.050	0.76	Solomon et al. [Solomon338]
	r_s [deg]	0.223	0.335	0.482	0.722	Solomon et al. [Solomon338]
	k_s/k_c	-0.068	-0.003	-0.037	-0.002	Croner and Kaplan [CRONER19957]
Contrast Normalization	r_{CN} [deg]	0.140	0.419	0.301	0.903	Bonin et al. [Bonin2005-cu]
	c_{50}	0.01	1.0	0.01	1.0	—
	n	0.01	1.0	0.01	1.0	—

Bayesian optimization. We employed Bayesian optimization using the `gp_minimize` function from the Scipy library [2020SciPy]. The optimization was performed over a defined parameter space for 640 evaluations, with 64 initial points generated using a Sobol sequence. The acquisition function was probabilistically selected among Lower Confidence Bound (LCB), Expected Improvement (EI), and Probability of Improvement (PI) at each iteration. The exploration-exploitation balance was controlled using $\kappa = 1.96$ for LCB and $\xi = 0.01$ for EI and PI.

E.3 Training Details

All models were trained on an internal cluster, using a 48GB NVIDIA A40 GPU with Python 3.11 and PyTorch 2.2+cu117, taking roughly tree days to train.

Preprocessing. During training, images were randomly horizontally flipped with a probability of 0.5, then resized and cropped to 224×224 pixels. For models without the SubcorticalBlock, images were normalized by subtracting and dividing by [0.5, 0.5, 0.5]. During evaluation, images were resized to 256 pixels on the shorter side, followed by a center crop to 224×224 pixels, and the same normalization was applied.

Loss function and optimization. Models were trained using a cross-entropy loss between ground-truth labels and predicted logits, with label smoothing [7780677] of 0.1. Optimization was performed using stochastic gradient descent with momentum set to 0.9 and weight decay of 5×10^{-4} . Training was conducted for 50 epochs with a batch size of 256. We employed the 1-Cycle learning rate policy [smith2018], where the learning rate was initialized at 0.004, increased to 0.1 at 30% of the total training steps, and then annealed to 4×10^{-7} following a cosine schedule. When using PRIME [10.1007/978-3-031-19806-9_36], we fine-tuned a standardly trained model for an additional 50 epochs using the same training protocol, except with a maximum learning rate of 0.01 reached at 10% of the training schedule.